Tight junctions potentiate the insulative properties of small CNS myelinated axons

Jerome Devaux[1,2] and Alexander Gow[3,4,5]

[1]Département Signalisation Neuronale, Le Centre de Recherche de Neurobiologie-Neurophysiologie de Marseille, Unités Mixtes de Recherche 6231, Centre National de la Recherche Scientifique, Université de la Méditerranée, Université Paul Cézanne, Institut Fédératif de Recherche Jean Roche, 13916, Marseille, Cedex 20, France
[2]Department of Neurology, University of Pennsylvania Medical Center, Philadelphia, PA 19104
[3]Center for Molecular Medicine and Genetics, [4]Carman and Ann Adams Department of Pediatrics, and [5]Department of Neurology, Wayne State University School of Medicine, Detroit, MI 48201

Claudin family proteins form the physical barriers of tight junctions (TJs) and regulate paracellular diffusion across polarized epithelia. In addition to these heterotypic TJs, claudin 11 forms autotypic TJs comprising the radial component of central nervous system myelin. The exact function of these TJs has been unclear, although their location at the membrane perimeter is well sited to regulate diffusion between the interstitium and intramyelinic space. In this study, we demonstrate that claudin 11 affords rapid nerve conduction principally for small diameter myelinated axons. *Claudin 11*–null mice have preserved myelin and axonal architecture, but as much as a 60% decrease in conduction. They also have increased action potential thresholds and activated internodal potassium channels. These data indicate that TJs modulate the biophysical properties of myelin. Computational modeling reveals that claudin 11 reduces current flow through myelin and moderates its capacitive charging. Together, our data shed new light on myelin structural components and our understanding of the biology and pathophysiology of this membrane.

Introduction

The ensheathment of neurons with myelin membrane is one of the key advances in vertebrate evolution (for review see Hartline and Colman, 2007) that has enabled rapid saltatory conduction, large reductions in axon diameter, and, ultimately, miniaturization of the central nervous system (CNS). Molecular and cell biology approaches over the last decade have unraveled several of the organizational and structural complexities of myelin sheaths that previously had been only glimpsed from morphological studies (for review see Schnapp and Mugnaini, 1978).

For example, the assembly of paranodal axoglial junctions (appearing as transverse bands in freeze-fracture replicas) requires association of the adhesion protein neurofascin-155 expressed by oligodendrocytes with the axonal caspr-contactin heteromer (Charles et al., 2002). Ablation of these junctions causes profound slowing of nerve conduction but minimally perturbs myelin compaction (Bhat et al., 2001; Boyle et al., 2001; Sherman et al., 2005). Together with evolutionary considerations (for review see Hartline and Colman, 2007), these data have led to the widespread notion that axoglial junctions form electrically tight barriers at paranodes to insulate the internodal axon segment, although the ultrastructure of transverse bands reveals an organization of intramembranous particles that is consistent with a permeable junction (Rosenbluth, 1999).

In contrast to axoglial junctions, the properties and functions of claudin 11 tight junctions (TJs) in CNS myelin are poorly understood. These junctions form the radial component observed in cross sections of CNS sheaths and may occlude the extracellular space at all noncompact myelin membrane surfaces (for review see Schnapp and Mugnaini, 1978; Peters, 1962). Early studies have suggested that TJs contribute to myelin stability or demarcate an immune privileged compartment to sequester myelin proteins (Mugnaini and Schnapp, 1974; Tabira et al., 1978). However, recent data from the lateral wall of the cochlear duct suggest a more traditional role for claudin 11 TJs

Correspondence to Alexander Gow: agow@med.wayne.edu

Abbreviations used in this paper: 4-AP, 4-aminopyridine; ACSF, artificial cerebrospinal fluid; AP, action potential; CAP, compound AP; CNS, central nervous system; CV, conduction velocity; DCM, double-cable model; DTX, dendrotoxin-1; MS, multiple sclerosis; PNS, peripheral nervous system; SHK, *Stichodactyla helianthus* toxin; TJ, tight junction; TJM, TJ model.

The online version of this article contains supplemental material.

The Rockefeller University Press $30.00
J. Cell Biol. Vol. 183 No. 5 909–921
www.jcb.org/cgi/doi/10.1083/jcb.200808034

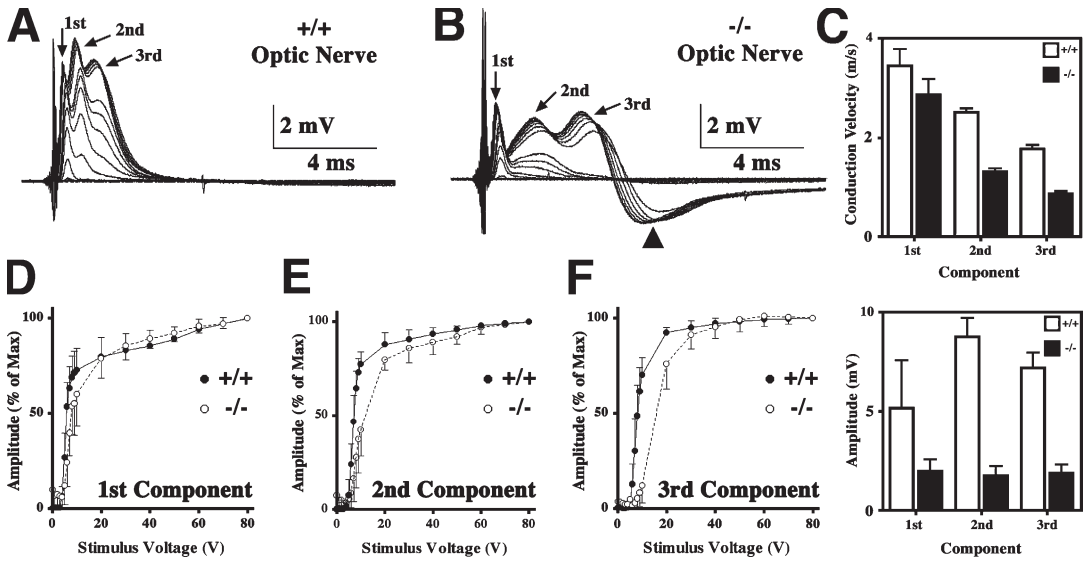

Figure 1. **CAPs in optic nerve from *Claudin 11*–null mice.** (A and B) Representative CAP series from optic nerves of wild-type (+/+) and *Claudin 11*–null (−/−) mice showing three components (arrows) elicited by square voltage pulses with varied amplitudes. (B) Arrowhead, hyperpolarizing afterpotential from −/− nerves. (C) CVs (top) and amplitudes (bottom) were measured at peak maxima (mean ± SD) from $n = 8$ (+/+) and $n = 7$ (−/−) optic nerves. (D–F) Axon recruitment profiles for each component. Greater voltages are required to recruit the majority of fibers from *Claudin 11*–null mice (open symbols) compared with controls (closed symbols). Error bars indicate SD.

in myelin physiology involving the generation and maintenance of chemical or electrical gradients (Gow et al., 2004; Kitajiri et al., 2004).

A detailed dissection of the physiological properties of myelin has been problematic, and this membrane is still viewed in a rudimentary manner as an amorphous stack of lipid bilayers (for review see Hartline and Colman, 2007; Waxman and Bennett, 1972). Computational models of myelinated fibers also reflect this simplistic view but reasonably account for its biophysical properties as an insulator with high resistance and low capacitance for large diameter fibers common to the peripheral nervous system (PNS). However, such models fall short in accounting for the properties of the small myelinated axons that are widely distributed in the CNS of humans and other mammals (Aboitiz et al., 1992; Rabi et al., 2007). Thus, current models may lack important structural features of CNS myelin sheaths.

In this study, we reveal novel functions and properties of two prominent structural components of murine myelinated fibers, TJs and axoglial junctions. First, an electrophysiological analysis in *Claudin 11*–null mice reveals severely slowed conduction velocities (CVs) and large juxtaparanodal potassium ion (K^+) currents in small diameter fibers. These abnormalities do not arise from disruptions to myelin structure or the partitioning of ion channels in axons but from changes in the biophysical properties of myelin. Second, we demonstrate that peptide toxins gain access to juxtaparanodal voltage-gated potassium channels (K_v) in wild-type and mutant mice, revealing the permeability of axoglial junctions to large molecules. To elaborate on our findings, we developed a novel computational model based on small CNS myelinated fibers (unpublished data). This model incorporates TJs into compact and noncompact myelin and accords with the electrophysiological analysis of *Claudin 11*–null mice to a greater extent than current models based on double-cable designs (Blight, 1985). Our data are significant in two respects. First, they demonstrate that a major function of claudin 11 TJs in the CNS is to form a series resistance with myelin membrane and impede its capacitive charge. This function has greater impact for small diameter myelinated axons than for large fibers. Second, they indicate that axoglial junctions may not form a permeability barrier at paranodes. Together, these data shed new light on the general principles of saltatory conduction with implications for neural coding in disease states.

Results

Slowed conduction in small optic nerve axons from *Claudin 11*–null mice

The measurement of compound action potentials (APs [CAPs]) in isolated optic nerves is an effective method for examining the function of CNS white matter tracts (Harroch et al., 2000). In adult rodents, extracellular recordings reveal three CAP components (Fig. 1 A, arrows) that are assumed to derive from large, medium, and small myelinated fibers conducting APs at different velocities (Freeman, 1978). These data are quantitatively similar to published values for adult wild-type mice (Rasband et al., 1999; Devaux et al., 2003).

The CAPs from age-matched *Claudin 11*–null mice also exhibit three components; however, several abnormalities are apparent (Fig. 1 B). First, latencies of the second and third CAP components are markedly increased with respect to controls, indicating slower nerve conduction in medium and small fibers. A statistical analysis (Fig. 1 C) indicates that CVs for these components are statistically different ($P < 0.01$) and approach 50% of normal, whereas the first component is minimally

slowed (P > 0.05). Second, recruitment of the second and third components is right shifted between 7 and 20 V, demonstrating increased thresholds for AP generation in small axons (Fig. 1, D–F). Third, amplitudes of the second and third CAP components are diminished in the mutants (P < 0.001), whereas the first component amplitude is unchanged (P > 0.05). These changes are not associated with nerve conduction block or shifts in the refractory period (Fig. S1, available at http://www.jcb.org/cgi/content/full/jcb.200808034/DC1), which are hallmarks of demyelination. Thus, likely causes include slowed CV, temporal dispersion, or hyperpolarizing afterpotentials (Fig. 1 B, arrowhead).

K^+ channels are activated in *Claudin 11*–null mice

Hyperpolarizing afterpotentials in the CAPs from mutant mice are strongly dependent on extracellular K^+ (Fig. 2), demonstrating that they are mediated by a K^+ conductance. Artificial cerebrospinal fluid (ACSF) used in the bath medium normally contains 3 mM KCl, and representative examples of the CAPs from wild-type (Fig. 2 A) and *Claudin 11*–null (Fig. 2 B) mice are shown. Decreasing extracellular KCl to 1 mM exacerbates hyperpolarization in the mutant optic nerves. Conversely, increasing the K^+ to 6 or 12 mM reduces or eliminates the afterpotentials. Changing extracellular K^+ has little effect on the wild-type CAPs (except at 12 mM K^+), and, together, these data suggest that K_v channel activity is increased in the mutant mice in association with the absence of myelin TJs.

To identify the K^+ conductance, we examined the effect on the CAPs of two channel-blocking agents. The K_v channel blocker dendrotoxin-1 (DTX) is a specific inhibitor of the juxtaparanodal channels $K_v1.1$ and $K_v1.2$ and does not perturb CAP latencies or shape in wild-type mice (Fig. 3 A, top). In contrast, DTX significantly affects *Claudin 11*–null optic nerves by increasing the amplitude of the third component and eliminating the afterpotentials (Fig. 3 A, bottom). These data demonstrate that $K_v1.1$ and $K_v1.2$ channels generate the hyperpolarizing afterpotentials in the absence of TJs.

Importantly, our data do not imply that TJs impede access of peptide neurotoxins to juxtaparanodal K^+ channels in wild-type fibers. Indeed, these channels reside in the axonal membrane and are sequestered underneath the myelin behind axoglial junctions, which are thought to serve as permeability barriers to the periaxonal space. However, the fluorescent conjugate 6-FAM-AEEAc–*Stichodactyla helianthus* toxin (SHK), which blocks $K_v1.1$ and $K_v1.2$ channels, readily diffuses through these junctions and binds to its targets in explants of adult wild-type mouse optic nerve (Fig. 3 B), *Claudin 11*–null optic nerve (not depicted), and rat spinal cord (Fig. S2, available at http://www.jcb.org/cgi/content/full/jcb.200808034/DC1). Thus, in contrast to published studies (for review see Hartline and Colman, 2007) suggesting that axoglial junctions serve as permeability barriers for the periaxonal space, our data show they are permeable to peptide toxins.

The broad spectrum membrane-permeant K^+ channel blocker 4-aminopyridine (4-AP) strongly increases amplitudes of the second and third components of the CAPs from *Claudin 11*–null mice (Fig. 3 A, bottom), which is consistent with the DTX data. Similar to earlier experiments (Devaux et al., 2003), 4-AP also broadens the CAPs in wild-type mice, indicating that K_v channels, possibly in the internode, are normally activated by APs in small fibers. The DTX and 4-AP inhibitors exert negligible effects on the latencies of CAP components (Fig. 3 C), indicating that K_v channel activity in the mutants does not directly cause conduction slowing. Furthermore, Western blots of $K_v1.1$ and $K_v1.2$ in the optic nerve show that K^+ channels are expressed at normal levels in *Claudin 11*–null mice (Fig. 3 D).

It is unlikely that the 4-AP response stems from inhibiting nodal channels such as $K_v3.1$ because of their low abundance in small CNS myelinated fibers (Devaux et al., 2003). Rather, the large effects of 4-AP (compared with DTX) on the $K_v1.1$ and $K_v1.2$ channels may stem from the small size and membrane-permeant properties of this inhibitor, which give it access to paranodal and internodal channels. Diffusion of DTX is more limited, and it would be unlikely to have significant access to internodal channels. However, we cannot preclude the possibility of other novel K_v channels in the nodes that are blocked by 4-AP.

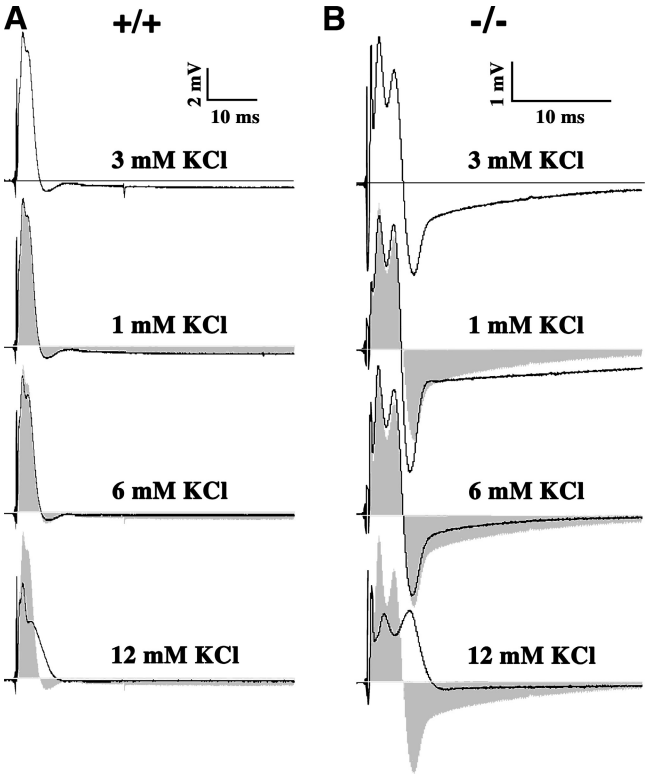

Figure 2. **The hyperpolarizing afterpotential is K^+ dependent.** (A and B) Representative optic nerve CAPs from wild-type (A) and *Claudin 11*–null mice (B) recorded for several concentrations of KCl in the bath solution ($n = 5$). ACSF solution normally contains 3 mM KCl. The hyperpolarization that follows the CAPs from −/− mice in ACSF is increased in low KCl (1 mM) and, reciprocally, decreased in high KCl (6 and 9 mM). In contrast, CAPs from +/+ mice are not affected by extracellular KCl concentrations between 1 and 6 mM. Gray shading represents the CAPs at 3 mM KCl.

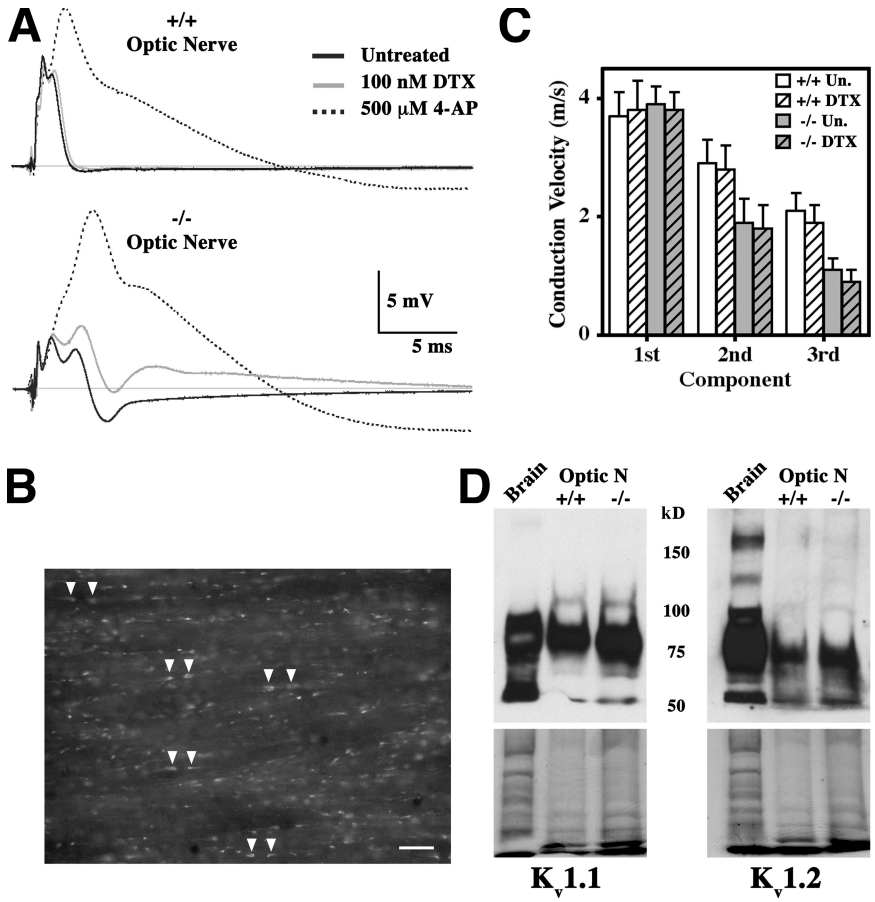

Figure 3. **Effects of K^+ channel blockers on optic nerves from *Claudin 11*–null mice.** (A) Representative CAPs from wild-type (top) and *Claudin 11*–null (bottom) mice treated with DTX or 4-AP in the bath medium. DTX broadens the CAPs only in −/− optic nerves. (B) Fluorescence image from a 10-μm frozen section of wild-type mouse optic nerve incubated with 6-FAM-SHK. The toxin has access to and labels juxtaparanodal $K_v1.1$ and $K_v1.2$ channels under the myelin sheaths in most axons (arrowheads). Nodes of Ranvier are unlabeled. Bar, 20 μm. (C) DTX has little effect on the CVs for each component (mean ± SD) in wild-type (+/+; $n = 5$) and *Claudin 11*–null (−/−; $n = 4$) mice. (D) Western blotting for $K_v1.1$ and $K_v1.2$ in single optic nerves show similar expression levels in +/+ and −/− mice after adjusting for protein loading (bottom; Coomassie blue R250–stained duplicate gels).

Nodal, paranodal, and juxtaparanodal myelin components are normally localized

Several studies demonstrate that perturbing the structural components of nodes, paranodes, and juxtaparanodes elicits strong behavioral phenotypes and abnormal CVs (Coetzee et al., 1996; Dupree et al., 1998; Bhat et al., 2001; Boyle et al., 2001; Sherman et al., 2005). Accordingly, we examined the organization of these components as well as voltage-gated sodium channels (Na_v) and K_v channels in optic nerve fibers from *Claudin 11*–null mice. Most importantly, we find that $K_v1.1$ and $K_v1.2$ channels are appropriately localized to juxtaparanodes and do not redistribute into nodes (Fig. 4, a–d). In addition, neurofascin-186 and $Na_v1.6$ channels are localized to nodes of Ranvier (Fig. 4, e, f, i, and j) and caspr, and neurofascin-155 and band 4.1 are appropriately localized at paranodes (Fig. 4, k–n). Together, these data indicate that the absence of TJs does not overtly alter or destabilize the organization of the node or the surrounding regions of myelin sheaths.

Myelin sheaths in *Claudin 11*–null mice are of normal length and thickness

To address the possibilities that shorter or thinner myelin sheaths might account for slower conduction in *Claudin 11*–null mice, we examined paranode density and *g* ratios in optic nerves. Comparable numbers of paranodes per field in micrographs are observed for wild-type and mutant mice (Fig. 4), indicating that sheaths are of relatively normal length.

The ultrastructure of optic nerve myelinated axons is preserved in adult *Claudin 11*–null mice (Fig. 5, A–D). Transverse sections of ferrocyanide-treated wild-type optic nerves show the locations of radial TJs in most myelinated fibers (Fig. 5 A, white arrowheads and arrows). These structures are absent in *Claudin 11*–null mice (Fig. 5 B); nonetheless, compact myelin morphology, axon shape, and axoplasmic composition are indistinguishable from controls. In longitudinal optic nerve sections (Fig. 5, C and D), paranodes of wild-type and mutant mice are morphologically similar, particularly with regard to axoglial junctions (Fig. 5, C and D; black arrowheads). We also find little evidence of overall changes in *g* ratios from the mutant nerves (Fig. 5 E). A frequency histogram of *g* ratios (Fig. 5 F and Table S1, available at http://www.jcb.org/cgi/content/full/jcb.200808034/DC1) reveals a small population of fibers with thicker than normal myelin in *Claudin 11*–null mice (lower *g* ratios); however, such changes are unlikely to decrease CV and cannot account for the electrophysiological changes we observe. The frequency distribution of axon diameters from mutant optic nerves is also very similar to controls (Fig. 5 G), indicating that CNS axons are not significantly perturbed by the absence of TJs.

Small myelinated fibers are affected by the absence of claudin 11 TJs

Our optic nerve CAP data reveal an important role for TJs predominantly in small caliber fibers. This is corroborated by recordings from ventral column explants of spinal cord, which

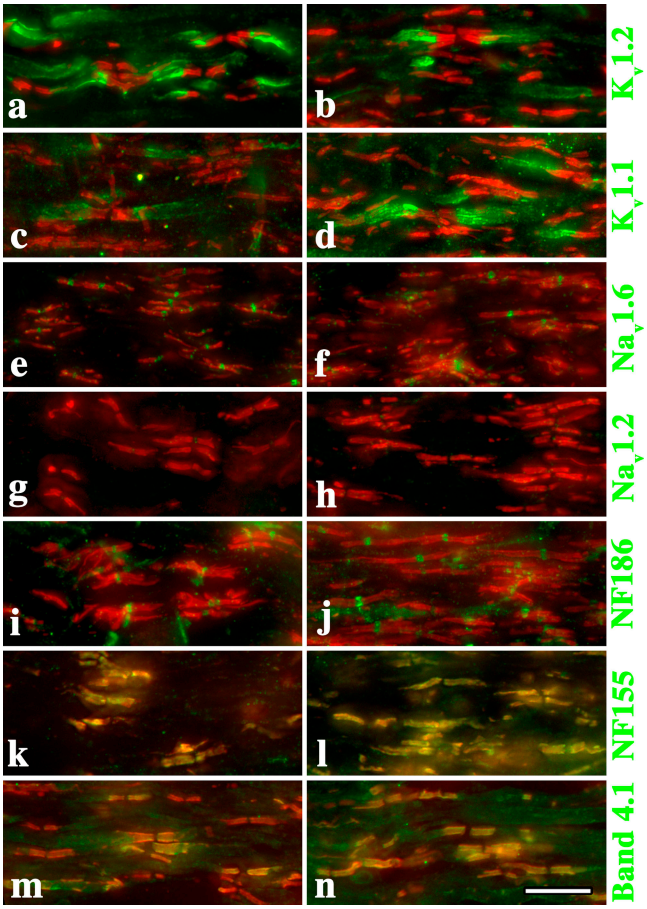

Figure 4. **Ion channels and structural components of the nodal region are appropriately localized in *Claudin 11*–null mice.** Cryostat sections of adult optic nerve from 2% PFA (in 0.1 M sodium phosphate buffer, pH 7.4) perfused wild-type (a, c, e, g, i, k, and m) and *Claudin 11*–null mice (b, d, f, h, j, l, and n). Antibody labeling shows that the major ion channels and structural components of nodes, paranodes, and juxtaparanodes are appropriately localized (green). Anti-caspr antibodies are used to label paranodes in all panels (red). Bar, 10 μm.

contain mostly large axons. Thus, the amplitude and shape of ventral column CAPs from *Claudin 11*–null mice are similar to controls and differ only by an increase in CAP duration (Fig. S3, A and B; and Table S2, available at http://www.jcb.org/cgi/content/full/jcb.200808034/DC1), which reflects slower conduction in the smallest myelinated axons. Furthermore, DTX does not alter the CAP amplitude (Fig. S3, A and B) in wild-type or *Claudin 11*–null mice, which is consistent with the analysis of the first component in optic nerves (Fig. 3). Similar to optic nerves, 4-AP increases the CAP amplitude in small diameter axons from wild-type and *Claudin 11*–null spinal cords. Finally, the recruitment and refractory period of *Claudin 11*–null spinal cord fibers are similar to controls (Fig. S3, C and D). Together, these data reveal the importance of claudin 11 for conduction in small fibers. In the absence of perturbed myelin morphology or redistribution of ion channels and other structural components in the nodes, we posit that TJs modify the biophysical properties of myelin by providing a barrier to radial current flow, thereby enhancing the insulative properties of small sheaths.

A novel computational model of optic nerve fibers incorporating TJs

To explore this hypothesis, we developed a computational TJ model (TJM) of CNS myelinated axons (unpublished data). This model is reminiscent of earlier double-cable model (DCM) designs that have been used to describe large fibers in the PNS and CNS (Halter and Clark, 1991; McIntyre et al., 2002), but it incorporates physical dimensions derived from optic nerve axons, experimentally determined conductances, and a TJ resistance in series with the axolemmal and myelin cables (see Materials and methods). The TJM is predicated on considering the myelin sheath as a modified polarized epithelium and satisfies five criteria that have been established empirically from electrophysiological and morphological data (Figs. 1–5): TJs enable conduction in axons of ∼0.5-μm diameter, TJs increase CV, TJs decrease AP threshold, TJs decrease juxtaparanodal K^+ channel activity, and TJ function is substantially more important for small axons than for larger axons. The suitability of the TJM in fulfilling these criteria is demonstrated in Fig. 6 in a head to head comparison with simulations from a DCM based on previous models (Halter and Clark, 1991; McIntyre et al., 2002) but with physical dimensions and passive properties identical to the TJM (Fig. 6).

Slower CVs in small fibers in the absence of TJs

To derive physiological data from the optic nerve CAPs for comparison with the computational models, we estimated the mean axonal diameter corresponding to each of the CAP components (Fig. 1, A and B) using the axon diameter frequency distributions in Fig. 5 G. Thus, for both wild-type and *Claudin 11*–null mice (Fig. S4 A, available at http://www.jcb.org/cgi/content/full/jcb.200808034/DC1), the first CAP component corresponds to an axon diameter of ∼2.1 μm, the second component to 1.2 μm, and the third to 0.7 μm. The mean CVs for each of these components (Fig. 1 C) is expressed as a ratio of *Claudin 11* null/wild type (CV^{TJ-}/CV^{TJ+}) and plotted as a function of axon diameter. These data highlight the strong reduction in CVs in the absence of TJs, particularly for small axons (Fig. 6 A, closed circles). Thus, CV in 0.7-μm axons is slowed by >50%, whereas the reduction is ∼20% for 2.1-μm axons.

Conduction slowing in TJM simulations for axons of 0.6–2.1-μm diameter (Fig. 6 A, open circles) closely fits the physiological data. DCM simulations also propagate APs over this range of axon diameters, and to determine whether the TJM data could arise from a simple decrease in myelin resistance, we reduced ρ_{my} in the DCM by 30 (DCM*a*) or 300% (DCM*b*). In both cases, the DCM data poorly fit the physiological data. In the latter case, axons <0.9 μm in diameter also do not propagate APs. However, increasing myelin resistance by 300% (DCM*c*; unpublished data) does not improve the fit, and the data are very similar to DCM*a*.

Increased AP thresholds in small fibers in the absence of TJs

Recruitment of myelinated fibers also can be modeled using the TJM and DCM. In simulations, we define recruitment as the

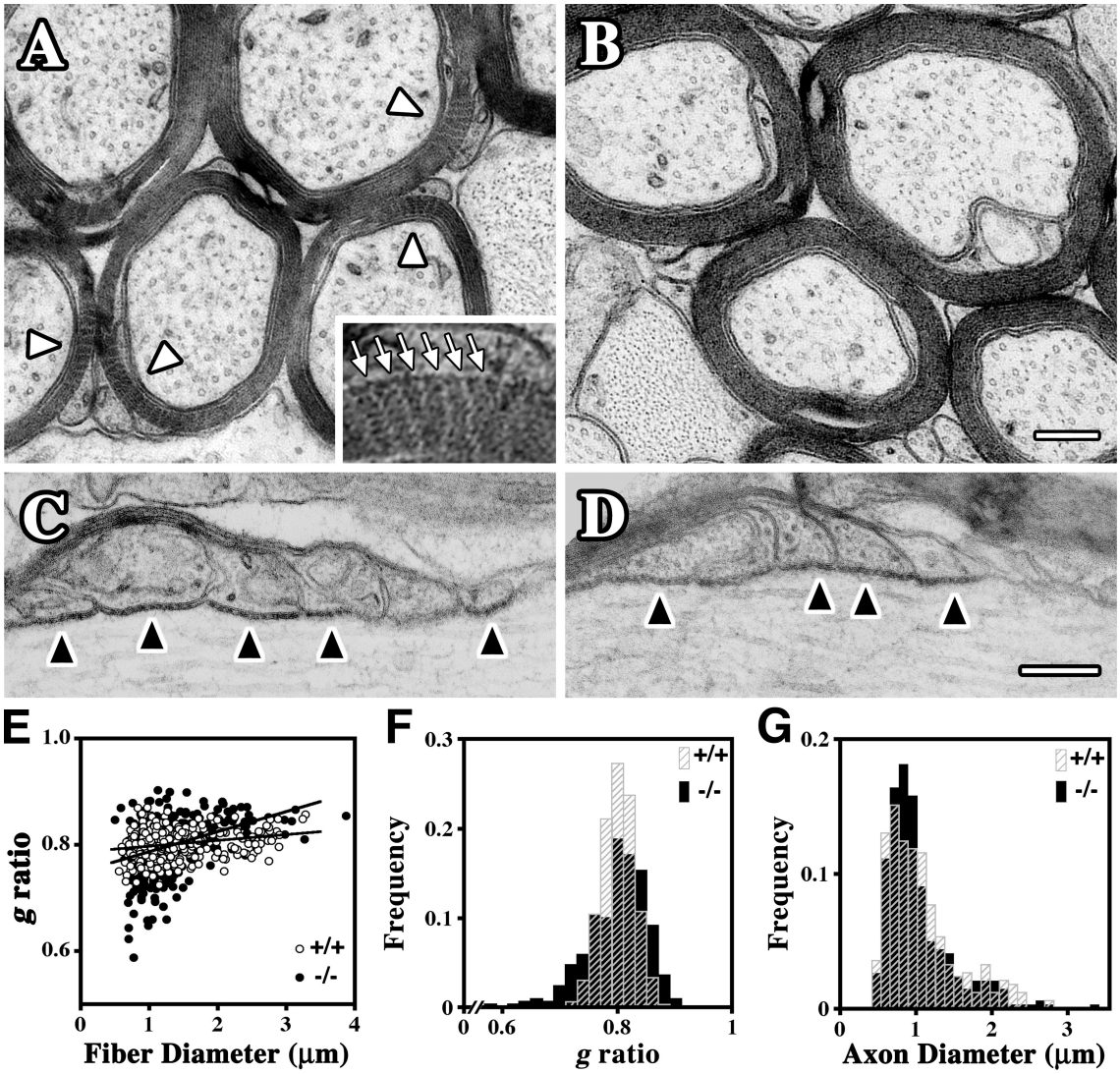

Figure 5. **Morphometric analysis of optic nerves from *Claudin 11*–null mice.** (A–D) Electron micrographs showing transverse (A and B) and longitudinal (C and D) sections of optic nerve from 3-mo-old wild-type (A and C) and *Claudin 11*–null (B and D) mice. Arrowheads in A point to the TJs (radial components), which appear as multiple white zigzag lines across the compact myelin. The inset shows TJs (arrows) at a threefold higher magnification. These structures are absent in *Claudin 11*–null mice. Normal axoglial junctions are present at paranodes in both wild-type and *Claudin 11*–null mice and appear as black dots in the extracellular space between the myelin loops and the axon (black arrowheads). Nodes of Ranvier are to the right in C and D. (E) *g* ratios derived from littermate wild-type (+/+) and *Claudin 11*–null (−/−) mice (three mice per genotype, 100 myelinated fibers per mouse) are plotted against fiber diameter. Linear regression lines are similar for each genotype. (F) Frequency histogram of *g* ratios from E highlights the similarity of the distributions for +/+ and −/− mice. Statistics for +/+, 0.80 ± 0.03 (mean ± SD) and −/−, 0.80 ± 0.05. (G) Frequency histogram of axon diameters measured in E shows the similarity in the distributions of axon diameters for +/+ and −/− mice. Bars, 0.2 μm.

minimum injected current (threshold) necessary to initiate an AP at the injected node. In the TJM, these thresholds are determined in the presence and absence of TJs and are expressed as the current ratio, I^{TJ-}/I^{TJ+}, plotted as a function of axon diameter (Fig. 6 B). We could not derive physiological data from the CAPs for comparison; however, it is clear that the absence of TJs in TJM simulations significantly increases the current threshold required to elicit an AP. Furthermore, the magnitude of the increase is axon diameter dependent and is greater for small fibers. In contrast, I^{TJ-}/I^{TJ+} ratios from the DCM for different values of ρ_{my} are close to unity and largely constant for different axon diameters, which is not consistent with the physiological data in Fig. 1 (D–F).

Increased juxtaparanodal K^+ currents in small fibers in the absence of TJs

The electrophysiology data in Figs. 2 and 3 indicate that K_v channels, most likely juxtaparanodal, are strongly activated in the absence of TJs. To determine whether the TJM can model these data, we measured the juxtaparanodal K^+ currents generated from propagating APs and plotted them as a function of axon diameter (Fig. 6 C). In the absence of TJs, the peak K^+ currents increase sharply as axon diameter decreases. TJs strongly suppress this activity in axons of ∼0.7–0.9-μm diameter, but their effectiveness is relatively modest in smaller fibers. Furthermore, TJs have little influence over K^+ currents in axons >0.9 μm, presumably because myelin thickness alone is sufficiently

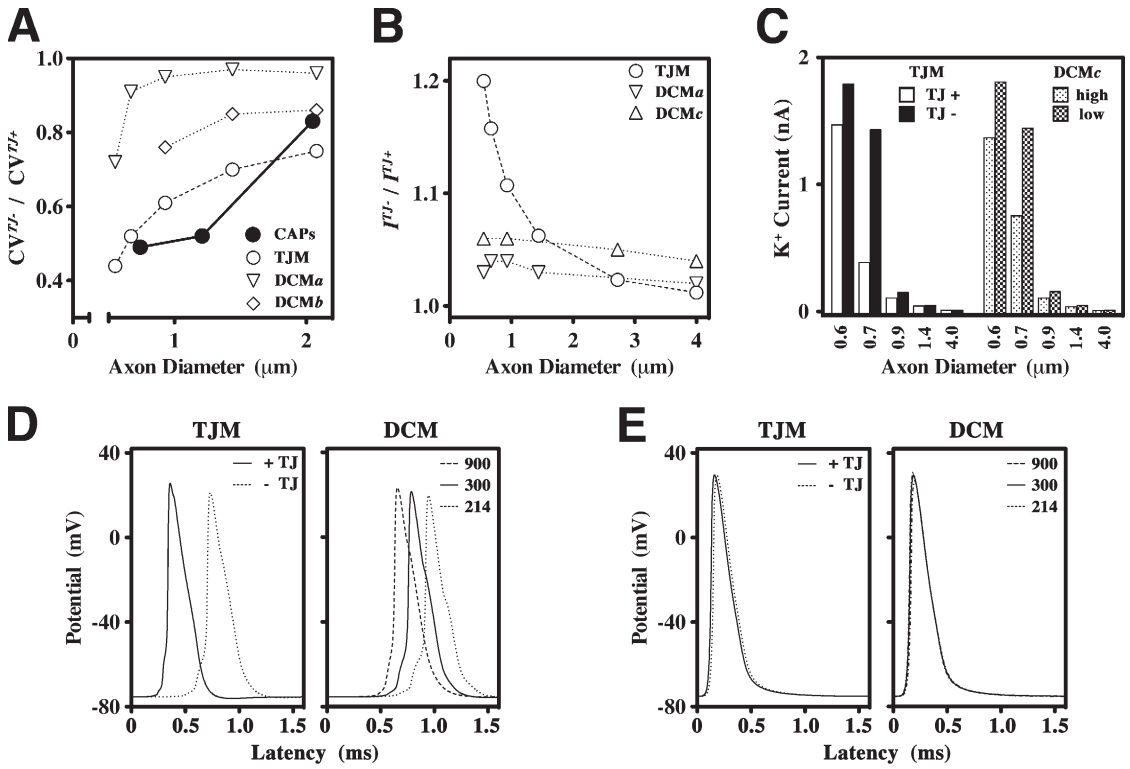

Figure 6. **Comparison of the TJM and DCM models.** (A) Ratios of CVs in the absence and presence of TJs (CV^{TJ-}/CV^{TJ+}) are plotted as a function of axon diameter for optic nerves from wild-type and *Claudin 11*–null mice (closed symbols). These data are compared with CV simulations from the TJM (unpublished data) and the DCM (Halter and Clark, 1991; McIntyre et al., 2002). The physical dimensions of myelin are calculated for axons of differing size and are identical for both the TJM and DCM. In the TJM, myelin resistivity, ρ_{my} = 300 Ohm.cm^2, is derived from the midpoint of the published (Tasaki, 1955; Barrett and Barrett, 1982; Blight, 1985) range of values (ρ_{my} = 100–1,000 Ohm.cm^2). The TJ resistivity in the TJM, ρ_{tj} = 600 Ohm.cm^2, is derived from comparison of the TJM to published data (Janecki et al., 1999) as well as to a detailed analysis of the model characteristics (unpublished data). We simulate the absence of TJs by reducing the value of ρ_{tj} 10-fold to 60 Ohm.cm^2. The DCM has no provision for adding or removing TJs; however, we have increased or decreased myelin resistance to test the effects on conduction of alterations in the biophysical properties of myelin. Thus, we define several conditions for comparing the TJM with the DCM. In DCM*a*, ρ_{my} = 300 Ohm.cm^2 is decreased by 30% (ρ_{my} = 214 Ohm.cm^2) to simulate the absence of TJs, which is the lowest value allowing 0.6-μm-diameter axons to propagate APs. In DCM*b*, ρ_{my} = 300 Ohm.cm^2 is decreased threefold. (B) The ratios of threshold currents, *I*, that elicit local APs at a node of Ranvier in the absence and presence of TJs (I^{TJ-}/I^{TJ+}) in myelinated fiber simulations (unpublished data) plotted as a function of axon diameter. Values of ρ_{my} and ρ_{tj} used in the TJM and DCM*a* are the same as in A. In DCM*c*, ρ_{my} = 300 Ohm.cm^2 is increased threefold. (C) Peak K^+ currents across the axonal membrane at the paranode–juxtaparanode boundary from TJM and DCM*c* simulations are plotted as a function of axon diameter. High, ρ_{my} = 900 Ohm.cm^2; low, ρ_{my} = 300 Ohm.cm^2. (D and E) APs generated in 0.6- (D) and 4-μm (E) axons by the TJM (left) in the presence and absence of TJs and by the DCM (right) using values for ρ_{my} corresponding to DCM*a*–*c*.

resistive to insulate the internodal axon. The DCM (DCM*c*) is comparable with the TJM for most axons except those around 0.7-μm diameter in which TJs in the TJM suppress K^+ currents more effectively than does a threefold increase in myelin resistance in the DCM. Indeed, myelin resistance would need to be increased >300-fold to approximate the effectiveness of TJs.

APs generated from the TJM and the DCM under most conditions used in Fig. 6 (A–C) are shown for 0.6- (Fig. 6 D) and 4.0-μm (Fig. 6 E) axons. For small axons, TJs decrease the latency of APs more effectively than does increasing myelin resistance in the DCM. Importantly, the duration of the APs at half-maximal voltage is not affected by the absence of TJs, which is consistent with the normal refractory period found in optic nerves of *Claudin 11*–null mice. However, several changes are apparent: the threshold of activation of the APs is greater in the absence of TJs, the peak amplitude is decreased, and depolarizing afterpotentials are larger. In contrast, removing TJs or reducing myelin resistance has a minimal effect on AP characteristics in large fibers.

Together, the data in Fig. 6 demonstrate that the TJM exhibits behavior that is similar in several respects to the electrophysiology data from *Claudin 11*–null optic nerves and superior to the DCM in most respects. The TJM satisfies five criteria: conduction in small fibers, the potentiating effect of TJs on CV, the reduction of AP thresholds by TJs, the suppression of juxtaparanodal K^+ currents by TJs, and the axon diameter–dependent behavior with stronger effects in small fibers.

Importance of internodal K^+ channels in minimizing depolarizing afterpotentials

The electrophysiology data in Fig. 3 demonstrate the importance of K^+ channels in shaping the late phase of APs by minimizing depolarizing afterpotentials in small diameter fibers (Fig. 3 A). The TJM simulations reproduce several aspects of the electrophysiology in Fig. 3. They demonstrate that K^+ channels underneath the myelin are normally active in small diameter axons irrespective of the presence or absence of TJs, TJs diminish K^+ channel activity in intermediate axons, and K^+ conductances have minimal influence on CV.

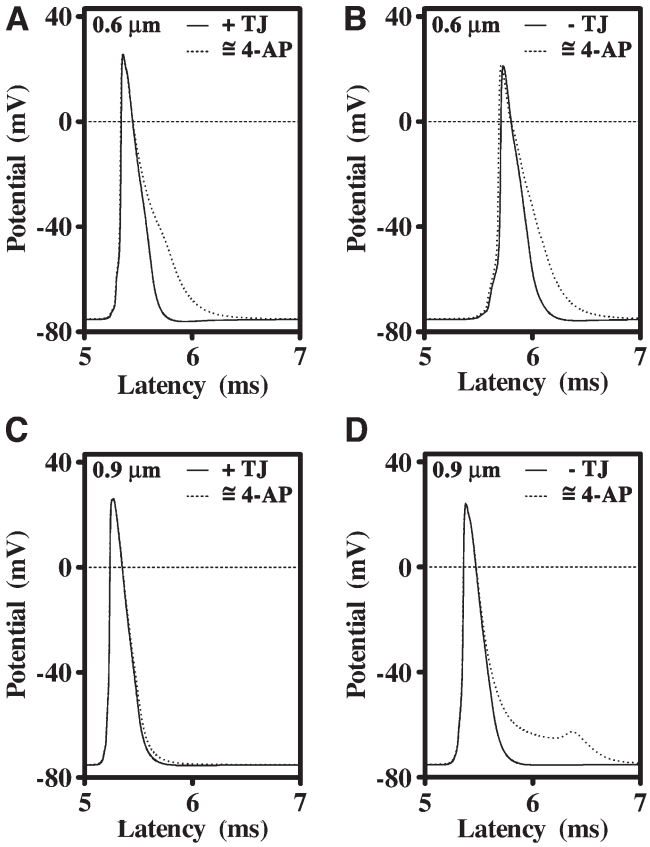

Figure 7. **Juxtaparanodal and internodal K^+ channels moderate the appearance of depolarizing afterpotentials.** (A) A 100-fold reduction in K^+ conductance from a 0.6-μm axon ensheathed with myelin containing TJs prolongs the late phase of the AP but does not change the latency of the AP. (B) In the absence of TJs, the AP propagates more slowly but is similarly broadened by a reduction in K^+ conductance. (C) Neither the shape nor latency of the AP from 0.9-μm axons is influenced by reducing the K^+ conductance in the presence of TJs. (D) In the absence of TJs, reducing the K^+ conductance elicits strong depolarizing afterpotential in 0.9-μm axons, indicating that depolarization of the juxtaparanodal and internodal axonal membranes is the likely cause of prominent K^+ channel activation in *Claudin 11*–null mice.

Fig. 7 A shows APs from a 0.6-μm-diameter axon (approximately equivalent to the third component in Fig. 3) ensheathed by wild-type myelin (+TJs) with either normal K^+ conductances in juxtaparanodal and internodal regions or 100-fold reductions in these conductances. The latter is intended to mimic the effect of 4-AP and shows that K_v channels normally curtail depolarizing afterpotentials in small axons. In the absence of TJs (Fig. 7 B), the blockade of the K^+ conductances also broadens the AP but does not affect its latency, as observed in vivo (Fig. 3 B).

For 0.9-μm wild-type axons (approximately equivalent to the second component in Fig. 3), the shape of the AP is not affected by a 100-fold reduction in K^+ channel conductance under the myelin (Fig. 7 C), which indicates that K_v channels are normally only marginally involved in repolarizing the AP. However, inhibiting K^+ channels in the absence of TJs substantially broadens the AP (Fig. 7 D) without affecting its latency. These data are consistent with the effects of 4-AP on the CAPs from *Claudin 11*–null and wild-type optic nerves and indicate that the function of juxtaparanodal K^+ channels is to moderate the appearance of delayed depolarizing afterpotentials. In the absence of TJs, the amplitude and duration of these depolarizing afterpotentials are increased, which accounts for the prominent K^+ channel activity observed in *Claudin 11*–null mice.

Discussion

In this study, we investigate the physiological function of claudin 11 TJs in myelin and describe a mechanism that accounts for the neurological phenotype in *Claudin 11*–null mice (Gow et al., 1999). The absence of myelin TJs does not perturb myelination, myelin ultrastructure, or myelin stability or result in immune-mediated (or nonimmune) demyelination. Rather, small axons propagate APs at significantly lower speeds than normal, whereas large axons with thicker myelin sheaths conduct relatively normally. Thus, this analysis reveals the unanticipated importance of TJs for saltatory conduction. Claudin 11 forms an electrically tight barrier that potentiates the insulative properties of CNS myelin sheaths; however, this potentiation is normally only significant for small axons with thin sheaths and is marginal for large axons. In addition, we demonstrate that axoglial junctions are permeable to soluble peptides, which suggests that they may not be electrically tight. Together, our findings have major impacts on our understanding of myelin biology during development, evolution, and neurological disease.

The function of claudin 11 TJs in myelin

At the earliest stages of myelinogenesis, claudin 11 localizes to the leading edges of the expanding myelin sheet, apparently forming a permeability or possibly an electrical barrier at contact points as they arise (unpublished data). Coincident to membrane tube expansion along the axon, the claudin 11 interface also extends along the membrane contact zone as a zipper (Gow et al., 1999). Conceivably, claudin 11 could serve an adhesive function, as has been suggested from early experiments of myelin structure (Tabira et al., 1978) and for other claudins (Nunes et al., 2006). However, there is little ultrastructural evidence in myelin of connections to the cytoskeleton that are typical of adhesive junctions. Moreover, cytoplasmic plaque proteins that recruit the cytoskeleton to adhesive junctions, such as the zonula occludens proteins, are absent in CNS myelin.

In *Claudin 11*–null mice, we demonstrate that CNS myelinogenesis proceeds normally but that small fibers exhibit increased AP thresholds and conduct slowly. Furthermore, we show that these electrophysiological abnormalities are associated with large K^+ conductances and depolarization of the internodal membrane; they are not attributable to changes in the Na_v channel subunit composition at nodes, changes in K_v channel density or localization, width of the paranodal periaxonal space, or altered axoglial junction assembly.

The mild phenotype of *Claudin 11*–null mice, which have a normal life span, is distinct from that of mice lacking axoglial junctions and is associated with a fine tremor and hind limb weakness. Currently, it is unclear to what extent these abnormalities are directly attributable to changes in the biophysical properties of myelin rather than to the absence of claudin 11 in other tissues (Gow et al., 1999); however, conceivably, they arise directly from slowed conduction in small myelinated axons

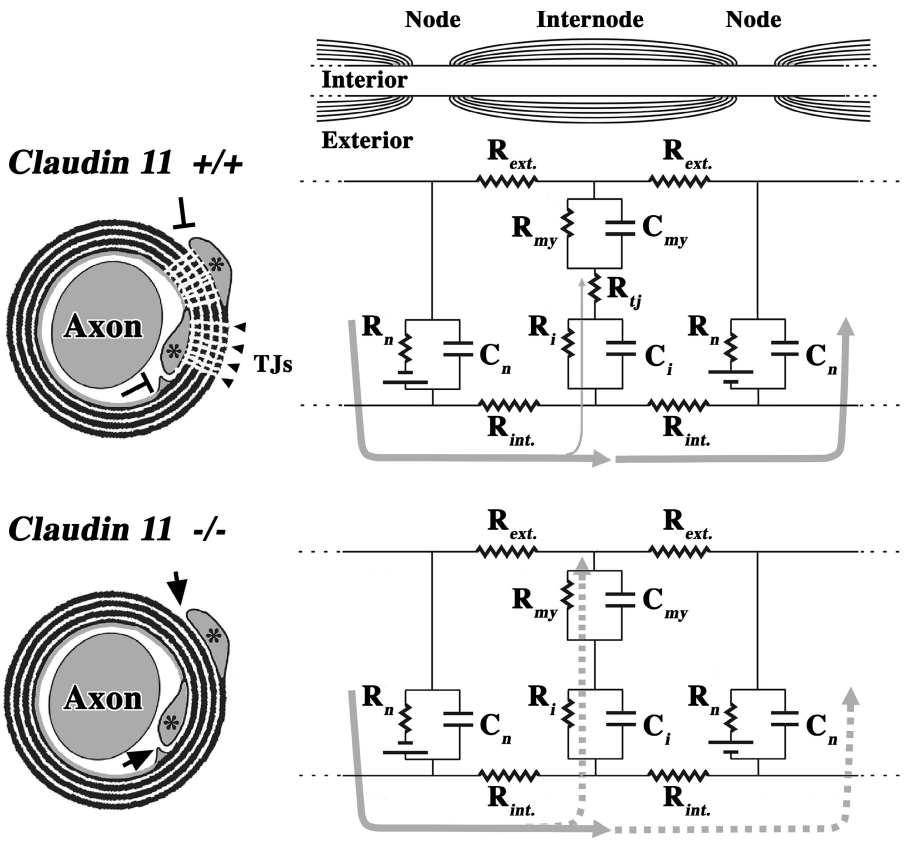

Figure 8. **Claudin 11 TJs generate an electrically tight barrier in myelin.** Transverse sections of myelinated axon best show the relationships between the axon, compact internodal myelin, and claudin 11 TJs. The inner and outer cytoplasmic loops (asterisks) are invested by TJs, which occlude entry zones into the extracellular compartment within the myelin sheath (T arrows). In the longitudinal section of a myelinated axon (top right), the equivalent circuit represents an AP spreading from one node (left) to the next, which is at rest (right). In a wild-type axon, most of the current (thick gray arrows) flows to the subsequent node, and only a small amount is dissipated through the myelin (thin gray arrows). For *Claudin 11*–null fibers, the myelin morphology is normal, but the radial TJs are absent, and entry zones into the compact internodal myelin are open (arrows). Consequently, the AP reaches the subsequent node (dashed gray arrows) but substantially depolarizes the internodal axonal membrane in the process and charges the myelin membrane. For clarity, axoglial junctions are not represented here. $R_{int.}$ and $R_{ext.}$, resistance of the axonal cytoplasm and extracellular space; R_{my} and C_{my}, resistance and capacitance of the myelin; R_{tj}, resistance of the TJs; R_n and C_n, resistance and capacitance of nodes of Ranvier; R_i and C_i, resistance and capacitance of the internodal axonal membrane.

of cerebellar Purkinje neurons and upper motor neurons of the corticospinal tract.

In contrast, the absence of axoglial junctions reduces or blocks conduction in all myelinated axons, resulting in severe CNS and PNS dysfunction and early death. Structural defects include the mislocalization of juxtaparanodal K_v channels to paranodes and nodes, the emergence of large K^+ currents, and significant increases in the width of the periaxonal space as paranodal myelin loops become everted with respect to the axon (Coetzee et al., 1996; Bhat et al., 2001; Boyle et al., 2001; Sherman et al., 2005). Myelin TJs remain intact in at least some of these mutants (Zonta et al., 2008), indicating that the observed conduction abnormalities stem from the axoglial junction defects.

From an evolutionary perspective, axoglial junctions (more generally known as septatelike junctions) and TJs have long been co-opted in the nervous system to serve as diffusion and possibly electrically tight barriers. For example, an antecedent of the caspr-containing mammalian axoglial junction, the neurexin IV–containing pleated septate junction of the *Drosophila melanogaster* blood–nerve barrier, is known to be impermeable to monovalent cations if not electrically tight (Baumgartner et al., 1996). This barrier is also dependent on the presence of the claudin family member sinuous for its structural organization and barrier properties (Wu et al., 2004); thus, it is unclear which pleated septate junction component confers barrier function.

Together, our data lead us to conclude that claudin 11 TJs form an electrically tight barrier in myelin, as in the cochlea (Gow et al., 2004; Kitajiri et al., 2004), and they complement the myelin membrane in preventing internodal depolarization. The model in Fig. 8 illustrates our view that axoglial junctions are not the only junctions involved in insulating the axon (for review see Hartline and Colman, 2007). Our finding that peptides are able to rapidly diffuse through axoglial junctions demonstrates that they do not form permeability barriers, but we do not know whether they are electrically tight. This issue not withstanding, our TJM simulations do indicate that myelin TJs function differently and independently of axoglial junctions (Fig. S4, B and C).

Implications for myelin TJs in remyelination

In this study, we have focused on the importance of claudin 11 for small myelinated axons in the adult nervous system. However, TJ function may be also relevant for large axons under circumstances in which myelin is thin, such as during myelin deposition in development or for remyelinated axons denuded during neurodegenerative disease. Although the former instance is transient, the latter is permanent and can have major consequences for CNS function.

For example, the pathophysiology of multiple sclerosis (MS) involves focal demyelination in white and gray matter regions of the CNS. The majority of these lesions are subsequently repaired by remyelination of denuded axonal segments, but repeated demyelination/remyelination cycles over many years may eventually result in the replacement of most myelin sheaths (Albert et al., 2007). Importantly, these secondary myelin sheaths rarely achieve the normal length and thickness of those generated during development, and remyelinated

cortical axons in MS patients may only reach 60–70% of normal thickness. In this light, an axon of 2.1-µm diameter ensheathed with 15 membrane wraps (the first component in Fig. 1) may achieve a myelin thickness of approximately nine wraps after remyelination (equivalent to the myelin thickness of the second component in Fig. 1). Thus, the range of axon diameters for which TJs are important for saltatory conduction is greater for demyelinating pathologies.

Implications for claudin 11 loss of function in other neurological diseases

Morphometric studies show that small diameter myelinated axons are widely distributed in the CNS of mammals, including humans (Aboitiz et al., 1992; Rabi et al., 2007). As summarized in Fig. S5 (available at http://www.jcb.org/cgi/content/full/jcb.200808034/DC1), 45–70% of myelinated axons in human corpus callosum are <1 µm in diameter, and we envisage that the absence of claudin 11 TJs would significantly lower CVs of most fibers in this white matter tract. Corpus callosum is the major conduit for interhemispheric communication, and small myelinated axons dominating the fiber population in anterior regions (e.g., the genu) mainly connect the prefrontal cortices, whereas those in posterior regions (anterior two-thirds of the splenium) connect the associative cortices (Hofer and Frahm, 2006).

The approximate length of collosal fibers in humans is 100–130 mm, and the transit time for APs through small diameter axons is 50–100 ms. A 40–60% reduction in CV in the absence of claudin 11 TJs would increase AP latencies by at least 20 ms, thereby perturbing information processing and integration in higher order cortical circuits with disastrous consequences for Hebbian long-term potentiation (Caporale and Dan, 2008). Thus, a *CLAUDIN 11* hypomorphic phenotype conceivably could include altered executive brain function, associative behavior, learning, and memory.

In this vein, several microarray studies show reduced expression of *CLAUDIN 11* and several other myelin-specific genes in cingulate and temporal cortices and the hippocampus in postmortem tissue from schizophrenia patients (Katsel et al., 2005; McCullumsmith et al., 2007). It is tempting to speculate that the disturbances in perception that feature in the clinical phenotype of schizophrenia may be in part associated with the distribution of small diameter myelinated fibers in the CNS. Interestingly, schizophrenia endophenotypes also are manifest in several demyelinating disorders, including metachromatic leukodystrophy, X-linked adrenoleukodystrophy, and MS, for which multifocal or diffuse myelin pathophysiology is known (Stewart and Davis, 2004). The convergent pathology in these diseases is thinner than normal myelin, which would reduce membrane resistance, increase capacitive charging of the myelin, and reduce CVs, perhaps analogously to the absence of claudin 11 TJs in *Claudin 11*–null mice. Thus, our analyses suggest a plausible link between congenital or acquired TJ dysfunction and several neurological disorders.

TJs in PNS myelin

The satisfying account of claudin 11 function in central myelinated fibers in this study has important implications for peripheral myelin. Schwann cells in the PNS localize claudin 19 TJs between paranodal loops, inner and outer mesaxons, and Schmidt-Lantermann incisures (Miyamoto et al., 2005). These sites are analogous to the locations of TJs in the CNS where the extracellular space around the entire perimeter of the myelin sheet is occluded. However, axons of <1-µm diameter that are most dependent on TJs in the CNS are rarely myelinated in the PNS (Waxman and Bennett, 1972); thus, it seems unlikely that PNS and CNS TJs function analogously. Indeed, several missense mutations identified in the human *CLAUDIN 19* gene are associated with renal failure and polycystic kidney disease but not with peripheral neuropathy (Konrad et al., 2006; Lee et al., 2006). Furthermore, nerve conduction measurements in sciatic nerves from *Claudin 19*–null mice (Miyamoto et al., 2005) fail to convincingly demonstrate slower than normal CVs.

Materials and methods

Animals

Claudin 11–null mice were generated as previously described (Gow et al., 1999) and maintained on an interbred 129 Sv/Ev-C57BL/6Tac background at Wayne State University facilities. These mice and wild-type littermates were used for experiment at 4–6 mo of age. Animals were handled and killed according to Wayne State University and University of Pennsylvania Institutional Animal Care and Use Committee guidelines.

Electrophysiology

Ventral columns from spinal cord were also recorded as described previously (Shi and Blight, 1996). In brief, animals were anesthetized with ketamine xylazine and perfused transcardially with oxygenated ice-cold ACSF containing 126 mM NaCl, 3 mM KCl, 2 mM $CaCl_2$, 2 mM $MgSO_4$, 1.25 mM NaH_2PO_4, 26 mM $NaHCO_3$, and 10 mM dextrose, pH 7.4–7.5, at 4°C equilibrated with 95% O_2/5% CO_2 (flow rate = 1–2 ml/min). The vertebral column was rapidly excised and transferred into oxygenated ice-cold ACSF, and the ventral white matter tracts were isolated with scissors (3-cm segment). After 60 min, ventral white matter tracts were placed in a triple-compartment recording chamber. The central compartment was perfused with ACSF (at 1–2 ml/min) equilibrated with 95% O_2/5% CO_2 at 35°C. The outer compartments were filled with ACSF containing 120 mM isotonic KCl and were isolated from the central compartment by a sucrose gap (isotonic sucrose solution perfused at 1 ml/min) and sealed with Vaseline. Electrodes were placed in the central and outer compartments to trigger and record CAPs. Optic nerves were quickly dissected from killed mice and transferred into ice-cold ACSF equilibrated with 95% O_2/5% CO_2 (flow rate = 1–2 ml/min). Optic nerves were allowed to equilibrate for 60 min in the chamber before electrophysiological measurement at 35°C, and suction electrodes were used to record CAPs (Devaux et al., 2002).

During experiments, white matter tracts were stimulated continuously with square wave pulses of 40-µs duration up to 80 V at a frequency of 0.25 Hz. Recorded signals were amplified, digitized at 500 kHz, and stored on a hard disk. Drugs were applied to the central compartment, and electrophysiological measurements were recorded after the effects of the drugs reached steady state, typically 30–60 min after application. DTX was purchased from Alomone Laboratories, and 4-AP was purchased from Sigma-Aldrich. For recruitment analysis, CAP amplitudes were measured and plotted as functions of stimulation intensity. Maximal amplitudes and area under the CAPs were measured, and the CAP delay and duration were calculated at half-maximal amplitude. For refractory period analysis, two successive stimuli were applied at variable delay intervals. The amplitude of the highest peak elicited by the second stimulus was measured and plotted as a function of the delay interval between the two stimuli.

EM

Mice were anesthetized with avertin and perfused with 0.9% NaCl followed by freshly prepared 2% PFA/0.5% glutaraldehyde in 0.2 M cacodylate buffer, pH 7.2, for 1 h. Optic nerves were kept overnight

in situ at 4°C and dissected, rinsed, and postfixed in 1% osmium in 0.15 M cacodylate buffer, pH 7.4. Alternately, 1.5% ferrocyanide was included with the osmium treatment to visualize the myelin TJs. Optic nerves were dehydrated with an ascending series of ethanol and embedded in epon. Thin sections were cut, stained with filtered lead citrate and uranyl acetate, and photographed at 8,000 *g* using a microscope (EM 1010; JEOL Ltd). Images in Fig. 5 have been contrast enhanced and sharpened using the unsharp mask tool (radius of 3.3 pixels) in Photoshop (CS2; Adobe).

Axon circumference and myelin thickness were measured from wild-type and *Claudin 11*–null littermate mice (three mice per genotype, 100 myelinated fibers per mouse) using the advanced measurements module in OpenLab (PerkinElmer), and *g* ratios were calculated (*g* ratio = axon diameter/fiber diameter).

Immunofluorescence

Mice were perfused with 4% PFA in 0.1 M sodium phosphate buffer, pH 7.2. Optic nerves and cervical spinal cords were dissected, cryoprotected, and embedded for cryostat sectioning. Cryostat sections are permeabilized with methanol for 10 min and blocked in 2% goat serum in TBS, pH 7.5, containing 1% bovine serum albumin and 0.1% gelatin.

The following overnight primary antibodies were used: guinea pig anti-caspr (1:500; Bhat et al., 2001), mouse anti-$Na_v1.2$ (1:250; Rasband et al., 1999), rabbit anti-$Na_v1.6$ (1:400; Rasband et al., 1999), rabbit anticontactin (1:500; Rios et al., 2000), rabbit anti-$K_v1.1$ (1:60; Alomone Laboratories), rabbit anti-$K_v1.2$ (1:60; Alomone Laboratories), rabbit anti–band 4.1β (1:1,000; Denisenko-Nehrbass et al., 2003), rabbit anti–neurofascin-186 (1:500; Southwood et al., 2004), and rabbit anti–neurofascin-155 (1:500; Southwood et al., 2004). Secondary antibodies were obtained from Jackson ImmunoResearch Laboratories, Invitrogen, and SouthernBiotech. Sections were visualized using a microscope (DMRA2; Leica). Photographs were captured through 100× 1.4 NA and 1.6× intermediate lenses using a digital camera (ER; Orca) driven by OpenLab software imported into Photoshop (CS2) as 16-bit grayscale files, combined, and the contrast was adjusted. Images were converted to 24-bit RGB and cropped.

6-FAM-SHK labeling

Freshly dissected optic nerves (unfixed) were incubated for 1 h into oxygenated ACSF maintained at 35°C and containing 500 nM 6-FAM-SHK (Bachem; Beeton et al., 2003). Optic nerves were rinsed three times in ACSF and quickly frozen in optimal cutting temperature, and 5–10-µm cryostat sections were cut, thaw mounted on glass slides, and cover slipped. Unfixed nonpermeabilized spinal cord sections were also labeled with 0.05–500 nM 6-FAM-SHK for 1 h in TBS containing 5% nonfat milk. Sections were visualized using a microscope (DMRA2) with a 63× 1.3 NA lens, and images were captured using a camera (Hamamatsu Photonics) driven by OpenLab (version 2.2). Images were contrast enhanced using Photoshop (CS2).

Western blotting

Optic nerves from wild-type and *Claudin 11*–null mice were diced into small pieces and dissolved in 5% SDS, 0.5% β-mercaptoethanol, 0.125 M Tris, pH 6.8, 20% sucrose, and bromophenol blue and heated to 90°C for 1 min. The insoluble material was removed by centrifugation at 10,000 rpm for 10 min. Protein concentrations were determined using a Bio-Rad Laboratories kit. Samples (100 µg of protein) were separated in a 7.5% SDS-PAGE gel (Laemmli, 1970) and were electrophoretically transferred to polyvinylidene difluoride membranes. After blocking with 5% nonfat milk in PBS for 1 h, the membranes were incubated with rabbit antibodies against $K_v1.1$ or $K_v1.2$ (1:1,000) at 4°C overnight, rinsed several times, and incubated with horseradish peroxidase–conjugated donkey anti–rabbit secondary antibody (1:5,000; Jackson ImmunoResearch Laboratories). Finally, the membranes were washed several times, and the signal was developed using ECL Plus (GE Healthcare) according to the manufacturer's instructions.

Computer simulations

The TJM and DCM simulations were developed in and implemented using the Neuron (version 6.1; http://www.neuron.yale.edu/neuron) simulation environment (Hines and Carnevale, 1997). In brief, the model comprises 20 myelin sheaths with 19 intervening nodes of Ranvier. Each sheath is subdivided into sections: eight paranodal, two juxtaparanodal, and one internodal. Published data reveal the linear relationships between axon diameter and several morphological features of myelin: paranode length, internode length, and myelin thickness (*g* ratio; for review see Hildebrand and Mohseni, 2005). These relationships are sufficient to derive our model for axons of differing size from 0.3- to 4-µm diameter. Physical dimensions for simulated axons were derived from morphometry in this study and from Southwood et al. (2004). Claudin 11 TJs are added as a resistance in series between the axon and myelin sheath. TJ resistivity is estimated to be ρ_{tj} = 600 Ohm.cm^2, both from the behavior of the TJM as well as empirical determinations from claudin 11 TJs in Sertoli cell cultures (Janecki et al., 1991). We simulated the absence of TJs in the TJM by reducing the resistivity 10-fold to ρ_{tj} = 60 Ohm.cm^2.

The characteristics of Na_v, fast K_v, slow K_v channels, leak currents, and their densities are derived from published studies (Frankenhaeuser and Huxley, 1964; Schwarz and Eikhof, 1987; Halter and Clark, 1991). The resting potential is set to 75 mV, and the temperature is 37°C. Integrations of differential algebraic equations are solved for variable time steps (absolute tolerance = 0.001) using the differential algebraic solver with preconditioned Krylov incorporated into the Neuron simulation environment.

CVs were derived from the latencies of APs propagated between 16 simulated myelin sheaths divided by the aggregate length of those sheaths. Current thresholds used in Fig. 6 B were derived iteratively by injecting square current pulses of varied amplitudes (100 µs) into node of Ranvier #9. The minimum current required to elicit an AP was defined as the threshold current, *I*. Peak juxtaparanodal K^+ currents elicited by a propagating AP (Fig. 6 C) were measured just distal to the paranode–juxtaparanode boundary at the proximal end of myelin sheath #5.

Statistical analyses

Data in this study are presented as means and standard deviations. Analysis of the CAP latencies was performed using an analysis of variance with Bonferroni posttests. Comparisons between other groups were performed using a Student's *t* test assuming two-tailed distributions and unequal variances. Differences are considered statistically significant at the $P < 0.05$ level.

Online supplemental material

Fig. S1 demonstrates that the *Claudin 11*–null phenotype is not a result of conduction block in the CNS. Fig. S2 shows that fluorescently labeled 6-FAM-SHK passes through the axoglial junctions in rat spinal cord myelinated fibers. Fig. S3 shows that CAPs in *Claudin 11*–null ventral spinal cords are only modestly slowed compared with controls and only in small fibers. In addition, the recruitment and refractory period are normal in the absence of TJs. Fig. S4 shows the analysis of axon diameter in the optic nerve of wild-type and *Claudin 11*–null mice for use in TJM and DCM simulations. In addition, TJM simulations reveal the dependence of CV in the absence of TJs as functions of axon diameter or resistance of axoglial junctions. Fig. S5 shows a morphometric analysis of the myelinated axon diameter distribution in human corpus callosum. Table S1 shows percentiles for the *g* ratio and axon diameter morphometric analyses in optic nerves from wild-type and *Claudin 11*–null mice. Table S2 shows quantitative characteristics of CAPs from spinal cord ventral columns of wild-type and *Claudin 11*–null mice. Online supplemental material is available at http://www.jcb.org/cgi/content/full/jcb.200808034/DC1.

We thank Ms. D. Bessert and C.M. Southwood for technical support. We are grateful for the tremendous support and guidance in all aspects of this work from Dr. S. Scherer. We also thank Drs. M. Hines and T. Carnevale and Drs. R. Andrade, R. Skoff, N. Davis, J. Li, and M. Shy for experimental techniques, helpful discussions, advice, and critical reading of the manuscript.

This work was supported by grants to J. Devaux from the Association Française contre les Myopathies and the National MS Society (RG3839A1/T), by grants to A. Gow from the National Institute on Deafness and Other Communication Disorders, the National Institutes of Health (DC006262), and the National MS Society (PP1372 and RG2891), and by grants to Dr. S. Scherer from the National Institute of Neurological Disorders and Stroke and the National Institutes of Health (NS 43174).

Submitted: 8 August 2008
Accepted: 30 October 2008

References

Aboitiz, F., A.B. Scheibel, R.S. Fisher, and E. Zaidel. 1992. Fiber composition of the human corpus callosum. *Brain Res.* 598:143–153.

Albert, M., J. Antel, W. Bruck, and C. Stadelmann. 2007. Extensive cortical remyelination in patients with chronic multiple sclerosis. *Brain Pathol.* 17:129–138.

Barrett, E.F., and J.N. Barrett. 1982. Intracellular recording from vertebrate myelinated axons: mechanism of the depolarizing afterpotential. *J. Physiol.* 323:117–144.

Baumgartner, S., J.T. Littleton, K. Broadie, M.A. Bhat, R. Harbecke, J.A. Lengyel, R. Chiquet-Ehrismann, A. Prokop, and H.J. Bellen. 1996. A *Drosophila* neurexin is required for septate junction and blood-nerve barrier formation and function. *Cell.* 87:1059–1068.

Beeton, C., H. Wulff, S. Singh, S. Botsko, G. Crossley, G.A. Gutman, M.D. Cahalan, M. Pennington, and K.G. Chandy. 2003. A novel fluorescent toxin to detect and investigate Kv1.3 channel up-regulation in chronically activated T lymphocytes. *J. Biol. Chem.* 278:9928–9937.

Bhat, M.A., J.C. Rios, Y. Lu, G.P. Garcia-Fresco, W. Ching, M.S. Martin, J. Li, S. Einheber, M. Chesler, J. Rosenbluth, et al. 2001. Axon-glia interactions and the domain organization of myelinated axons requires neurexin iv/caspr/paranodin. *Neuron.* 30:369–383.

Blight, A.R. 1985. Computer simulation of action potentials and afterpotentials in mammalian myelinated axons: the case for a lower resistance myelin sheath. *Neuroscience.* 15:13–31.

Boyle, M.E., E.O. Berglund, K.K. Murai, L. Weber, E. Peles, and B. Ranscht. 2001. Contactin orchestrates assembly of the septate-like junctions at the paranode in myelinated peripheral nerve. *Neuron.* 30:385–397.

Caporale, N., and Y. Dan. 2008. Spike timing-dependent plasticity: a Hebbian learning rule. *Annu. Rev. Neurosci.* 31:25–46.

Charles, P., S. Tait, C. Faivre-Sarrailh, G. Barbin, F. Gunn-Moore, N. Denisenko-Nehrbass, A.M. Guennoc, J.A. Girault, P.J. Brophy, and C. Lubetzki. 2002. Neurofascin is a glial receptor for the paranodin/Caspr-contactin axonal complex at the axoglial junction. *Curr. Biol.* 12:217–220.

Coetzee, T., N. Fujita, J. Dupree, R. Shi, A. Blight, K. Suzuki, and B. Popko. 1996. Myelination in the absence of galactocerebroside and sulfatide: normal structure with abnormal function and regional instability. *Cell.* 86:209–219.

Denisenko-Nehrbass, N., K. Oguievetskaia, L. Goutebroze, T. Galvez, H. Yamakawa, O. Ohara, M. Carnaud, and J.A. Girault. 2003. Protein 4.1B associates with both Caspr/paranodin and Caspr2 at paranodes and juxtaparanodes of myelinated fibres. *Eur. J. Neurosci.* 17:411–416.

Devaux, J., M. Gola, G. Jacquet, and M. Crest. 2002. Effects of K+ channel blockers on developing rat myelinated CNS axons: identification of four types of K+ channels. *J. Neurophysiol.* 87:1376–1385.

Devaux, J., G. Alcaraz, J. Grinspan, V. Bennett, R. Joho, M. Crest, and S.S. Scherer. 2003. Kv3.1b is a novel component of CNS nodes. *J. Neurosci.* 23:4509–4518.

Dupree, J.L., T. Coetzee, A. Blight, K. Suzuki, and B. Popko. 1998. Myelin galactolipids are essential for proper node of Ranvier formation in the CNS. *J. Neurosci.* 18:1642–1649.

Frankenhaeuser, B., and A.F. Huxley. 1964. The action potential in the myelinated nerve fiber of *Xenopus laevis* as computed on the basis of voltage clamp data. *J. Physiol.* 171:302–315.

Freeman, B. 1978. Myelin sheath thickness and conduction latency groups in the cat optic nerve. *J. Comp. Neurol.* 181:183–196.

Gow, A., C.M. Southwood, J.S. Li, M. Pariali, G.P. Riordan, S.E. Brodie, J. Danias, J.M. Bronstein, B. Kachar, and R.A. Lazzarini. 1999. CNS myelin and sertoli cell tight junction strands are absent in *Osp/Claudin 11*-null mice. *Cell.* 99:649–659.

Gow, A., C. Davies, C.M. Southwood, G. Frolenkov, M. Chrustowski, L. Ng, D. Yamauchi, D.M. Marcus, and B. Kachar. 2004. Deafness in *Claudin 11*-null mice reveals the critical contribution of basal cell tight junctions to stria vascularis function. *J. Neurosci.* 24:7051–7062.

Halter, J.A., and J.W. Clark Jr. 1991. A distributed-parameter model of the myelinated nerve fiber. *J. Theor. Biol.* 148:345–382.

Harroch, S., M. Palmeri, J. Rosenbluth, A. Custer, M. Okigaki, P. Shrager, M. Blum, J.D. Buxbaum, and J. Schlessinger. 2000. No obvious abnormality in mice deficient in receptor protein tyrosine phosphatase beta. *Mol. Cell. Biol.* 20:7706–7715.

Hartline, D.K., and D.R. Colman. 2007. Rapid conduction and the evolution of giant axons and myelinated fibers. *Curr. Biol.* 17:R29–R35.

Hildebrand, C., and S. Mohseni. 2005. The structure of myelinated axons in the CNS. *In* Multiple Sclerosis as a Neuronal Disease. S.G. Waxman, editor. Elsevier Academic Press, Boston. 1–28.

Hines, M.L., and N.T. Carnevale. 1997. The NEURON simulation environment. *Neural Comput.* 9:1179–1209.

Hofer, S., and J. Frahm. 2006. Topography of the human corpus callosum revisited–comprehensive fiber tractography using diffusion tensor magnetic resonance imaging. *Neuroimage.* 32:989–994.

Janecki, A., A. Jakubowiak, and A. Steinberger. 1991. Regulation of transepithelial electrical resistance in two-compartment sertoli cell cultures: in vitro model of the blood-testis barrier. *Endocrinology.* 129:1489–1496.

Katsel, P., K.L. Davis, and V. Haroutunian. 2005. Variations in myelin and oligodendrocyte-related gene expression across multiple brain regions in schizophrenia: a gene ontology study. *Schizophr. Res.* 79:157–173.

Kitajiri, S., T. Miyamoto, A. Mineharu, N. Sonoda, K. Furuse, M. Hata, H. Sasaki, Y. Mori, T. Kubota, J. Ito, et al. 2004. Compartmentalization established by claudin-11-based tight junctions in stria vascularis is required for hearing through generation of endocochlear potential. *J. Cell Sci.* 117:5087–5096.

Konrad, M., A. Schaller, D. Seelow, A.V. Pandey, S. Waldegger, A. Lesslauer, H. Vitzthum, Y. Suzuki, J.M. Luk, C. Becker, et al. 2006. Mutations in the tight-junction gene claudin 19 (CLDN19) are associated with renal magnesium wasting, renal failure, and severe ocular involvement. *Am. J. Hum. Genet.* 79:949–957.

Laemmli, U.K. 1970. Cleavage of structural proteins during the assembly of the head of bacteriophage T4. *Nature.* 227:680–685.

Lee, N.P., M.K. Tong, P.P. Leung, V.W. Chan, S. Leung, P.C. Tam, K.W. Chan, K.F. Lee, W.S. Yeung, and J.M. Luk. 2006. Kidney claudin-19: localization in distal tubules and collecting ducts and dysregulation in polycystic renal disease. *FEBS Lett.* 580:923–931.

McCullumsmith, R.E., D. Gupta, M. Beneyto, E. Kreger, V. Haroutunian, K.L. Davis, and J.H. Meador-Woodruff. 2007. Expression of transcripts for myelination-related genes in the anterior cingulate cortex in schizophrenia. *Schizophr. Res.* 90:15–27.

McIntyre, C.C., A.G. Richardson, and W.M. Grill. 2002. Modeling the excitability of mammalian nerve fibers: influence of afterpotentials on the recovery cycle. *J. Neurophysiol.* 87:995–1006.

Miyamoto, T., K. Morita, D. Takemoto, K. Takeuchi, Y. Kitano, T. Miyakawa, K. Nakayama, Y. Okamura, H. Sasaki, Y. Miyachi, et al. 2005. Tight junctions in Schwann cells of peripheral myelinated axons: a lesson from claudin-19–deficient mice. *J. Cell Biol.* 169:527–538.

Mugnaini, E., and B. Schnapp. 1974. Possible role of zonula occludens of the myelin sheath in demyelinating conditions. *Nature.* 251:725–727.

Nunes, F.D., L.N. Lopez, H.W. Lin, C. Davies, R.B. Azevedo, A. Gow, and B. Kachar. 2006. Distinct subdomain organization and molecular composition of a tight junction with adherens junction features. *J. Cell Sci.* 119:4819–4827.

Peters, A. 1962. Plasma membrane contacts in the central nervous system. *J. Anat.* 96:237–248.

Rabi, S., C. Madhavi, B. Antonisamy, and R. Koshi. 2007. Quantitative analysis of the human corpus callosum under light microscopy. *Eur. J. Anat.* 11:95–100.

Rasband, M.N., E. Peles, J.S. Trimmer, S.R. Levinson, S.E. Lux, and P. Shrager. 1999. Dependence of nodal sodium channel clustering on paranodal axoglial contact in the developing CNS. *J. Neurosci.* 19:7516–7528.

Rios, J.C., C.V. Melendez-Vasquez, S. Einheber, M. Lustig, M. Grumet, J. Hemperly, E. Peles, and J.L. Salzer. 2000. Contactin-associated protein (Caspr) and contactin form a complex that is targeted to the paranodal junctions during myelination. *J. Neurosci.* 20:8354–8364.

Rosenbluth, J. 1999. A brief history of myelinated nerve fibers: one hundred and fifty years of controversy. *J. Neurocytol.* 28:251–262.

Schnapp, B., and E. Mugnaini. 1978. Membrane architecture of myelinated fibers as seen by freeze-fracture. *In* Physiology and Pathobiology of Axons. S.G. Waxman, editor. Raven Press, New York. 83–123.

Schwarz, J.R., and G. Eikhof. 1987. Na currents and action potentials in rat myelinated nerve fibres at 20 and 37 degrees C. *Pflugers Arch.* 409:569–577.

Sherman, D.L., S. Tait, S. Melrose, R. Johnson, B. Zonta, F.A. Court, W.B. Macklin, S. Meek, A.J. Smith, D.F. Cottrell, and P.J. Brophy. 2005. Neurofascins are required to establish axonal domains for saltatory conduction. *Neuron.* 48:737–742.

Shi, R., and A.R. Blight. 1996. Compression injury of mammalian spinal cord in vitro and the dynamics of action potential conduction failure. *J. Neurophysiol.* 76:1572–1580.

Southwood, C., C. He, J. Garbern, J. Kamholz, E. Arroyo, and A. Gow. 2004. CNS myelin paranodes require Nkx6-2 homeoprotein transcriptional activity for normal structure. *J. Neurosci.* 24:11215–11225.

Stewart, D.G., and K.L. Davis. 2004. Possible contributions of myelin and oligodendrocyte dysfunction to schizophrenia. *Int. Rev. Neurobiol.* 59:381–424.

Tabira, T., M.J. Cullen, P.J. Reier, and H. Webster. 1978. An experimental analysis of interlamellar tight junctions in amphibian and mammalian C.N.S. myelin. *J. Neurocytol.* 7:489–503.

Tasaki, I. 1955. New measurements of the capacity and the resistance of the myelin sheath and the nodal membrane of the isolated frog nerve fiber. *Am. J. Physiol.* 181:639–650.

Waxman, S.G., and M.V. Bennett. 1972. Relative conduction velocities of small myelinated and non-myelinated fibres in the central nervous system. *Nat. New Biol.* 238:217–219.

Wu, V.M., J. Schulte, A. Hirschi, U. Tepass, and G.J. Beitel. 2004. Sinuous is a *Drosophila* claudin required for septate junction organization and epithelial tube size control. *J. Cell Biol.* 164:313–323.

Zonta, B., S. Tait, S. Melrose, H. Anderson, S. Harroch, J. Higginson, D.L. Sherman, and P.J. Brophy. 2008. Glial and neuronal isoforms of Neurofascin have distinct roles in the assembly of nodes of Ranvier in the central nervous system. *J. Cell Biol.* 181:1169–1177.